Accepted Manuscript

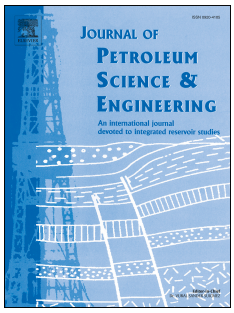

3D pore network extraction in granular media by unifying the Delaunay tessellation and maximal ball methods

Z. Li, Y.H. Wang, J.K. Chow, Z. Su, X. Li

PII: S0920-4105(18)30364-4

DOI: 10.1016/j.petrol.2018.04.058

Reference: PETROL 4910

To appear in: *Journal of Petroleum Science and Engineering*

Received Date: 13 October 2017

Revised Date: 18 March 2018

Accepted Date: 25 April 2018

Please cite this article as: Li, Z., Wang, Y.H., Chow, J.K., Su, Z., Li, X., 3D pore network extraction in granular media by unifying the Delaunay tessellation and maximal ball methods, *Journal of Petroleum Science and Engineering* (2018), doi: 10.1016/j.petrol.2018.04.058.

This is a PDF file of an unedited manuscript that has been accepted for publication. As a service to our customers we are providing this early version of the manuscript. The manuscript will undergo copyediting, typesetting, and review of the resulting proof before it is published in its final form. Please note that during the production process errors may be discovered which could affect the content, and all legal disclaimers that apply to the journal pertain.

ACCEPTED MANUSCRIPT

3D Pore Network Extraction in Granular Media by Unifying the Delaunay Tessellation and Maximal Ball Methods

Z. LI, Y. H. WANG, J. K. CHOW, Z. SU and X. LI

Submitted to *J. Pet. Sci. Eng.*

Zhaofeng LI
Postdoctoral fellow, Department of Civil and Environmental Engineering
The Hong Kong University of Science and Technology, Clear Water Bay, Hong Kong.
Email: zlibi@connect.ust.hk

Yu-Hsing WANG
Professor, Department of Civil and Environmental Engineering
The Hong Kong University of Science and Technology, Clear Water Bay, Hong Kong.
Email: ceyhwang@ust.hk

Jun Kang CHOW
Research Student, Department of Civil and Environmental Engineering
The Hong Kong University of Science and Technology, Clear Water Bay, Hong Kong.
junkangchow@gmail.com

Zhaoyu SU
Research Student, Department of Civil and Environmental Engineering
The Hong Kong University of Science and Technology, Clear Water Bay, Hong Kong.
Email: zsuad@connect.ust.hk

Xia LI
Professor, School of Civil Engineering
Southeast University, No. 2 Sipailou, Nanjing 210096, Jiangsu, China.
xia.li@seu.edu.cn

ACCEPTED MANUSCRIPT

ACCEPTED MANUSCRIPT

Corresponding author:
Yu-Hsing WANG, Professor
Department of Civil and Environmental Engineering
The Hong Kong University of Science and Technology
HKSAR, China.
Email: ceyhwang@ust.hk, Tel: (852) 2358-8757, Fax: (852) 2358-1534

Abstract: 210
Text: 4515
Tables: 1
Figures: 13

ACCEPTED MANUSCRIPT

ACCEPTED MANUSCRIPT

Abstract

In this study, a novel method for pore network extraction in the weakly consolidated media is reported, which unifies both the Delaunay tessellation (DT) and maximal ball (MB) methods in a complementary way. This unified method retains the advantages of both methods, and most importantly, eliminates the disadvantages when either the DT or the MB method is used individually. As a result of such a combination, the merging process of the Delaunay tetrahedra can be carried out in an objective way by utilizing the clustering results of maximal balls. Furthermore, the problems generated in using the maximal balls method, e.g., underestimating the throat size and producing tiny and incorrect throats, can be eliminated by incorporating the Delaunay tessellation, which enables precisely partition the pore space and accurately defining the throat size. Examination of this unified method, based on the results of pore network extraction on a sample (with a periodic boundary) before and after the triaxial shearing using DEM simulation, verifies that this method is objective and effective. The associated morphology of the pore space therefore can be accurately described in terms of the pore size, throat size and the associated distributions. This unified method also has the potential to characterize another dimension of fabric in granular media, i.e., the throat-based fabric.

Keyword: pore network extraction; Delaunay tessellation; maximal ball; DEM simulation.

ACCEPTED MANUSCRIPT

1. Introduction

Characterizing fluid transport through porous granular media, especially the weakly consolidated media, is of great importance in numerous disciplines, and understanding the associated behavior is the key to tackle various kinds of inherent problems, such as producing oil from petroleum bearing reservoirs (Dullien 1992; Coop and Willson 2003; Ghanizadeh et al. 2015; Rashid et al. 2012), internal erosion in earth structures (Reboul et al. 2010), clogging during hydrate formation (Kang et al. 2016), retarding the migration of radionuclide from a waste repositories (Bourg et al. 2003; Xiong et al. 2016), degradation of building materials (Wang et al. 2016), and many others. Using either experimentation (David et al. 1994; Zhu and Wong 1997; Meng et al. 2015) or multiscale simulation (Rong et al. 2013; Sun et al. 2016; Cui et al. 2016; Niu et al. 2017), the transport properties (e.g., the hydraulic conductivity) have been found to be intimately related to the features of the porosity and the stress state. Essentially, these two features first influence the morphology and topology of the pore space, and then affect the transport properties (Silin et al. 2004). In this regard, different attempts have also been made to explore the relationship between the internal pore structure and the transport properties, e.g., the permeability relations to the throat size (Rezaee et al. 2006; Gao and Hu 2013; Lala and EI-Sayed 2017), pore size (Burdine 1953; Juang and Holtz 1986) and tortuosity (Burdine 1953; Fishman and Bazylak 2011; Ghassemi et al. 2011). The validity of these research findings relies on a proper and precise description of the pore space, including knowing the features of the pores and throats. However, under a three-dimensional (3D) condition, the definitions of the pore and throat remain inconclusive, and most importantly, how to segment the pore space into pores and throats in an objective and more accurate way has not been accomplished yet.

Currently, there are two major approaches for the pore-network extraction in the weakly consolidated media, i.e., the Delaunay tessellation (DT) and maximal ball (MB) methods. Table 1 briefly describes these two methods and summarizes the associated advantages and disadvantages. The DT method is often used for samples with known particle/grain positions, for instance, the ideal samples generated in the DEM (discrete element method) simulations (Byrant and Blunt 1992; Al-Raoush et al. 2003; Gladkikh and Byrant 2006; Reboul et al. 2008; Shi et al. 2013; van der Linden et al. 2016; Das and Kumar 2017). It is also applicable to real unconsolidated samples, as individual particles and their positions in the tomography image could be easily identified using algorithms such as in Garboczi (2002) and Thompson et al. (2006). In the DT method, as shown in Figs. 1a and 1b, Delaunay tessellation is first constructed on the particle centroids. Then, the adjacent Delaunay tetrahedra are merged together when the common face is not considered as a void cell boundary, for instance, when the areal porosity of the common face, n (defined in Fig. 1c), exceeds a user-defined threshold, e.g., the value of n = 0.4 adopted in van der Linden et al. (2016). Note that different criteria to merge the Delaunay tetrahedra have also been proposed, for example in Al-Raoush et al. (2003) and Reboul et al. (2010). The whole space ultimately can be partitioned into different polyhedral void cells, each of which encloses a pore, and the associated throats pass through the common faces between the void cells (see Fig. 1d). As summarized in Table 1, the DT method can precisely partition the pore space to set the boundary between the pores and to satisfactorily define the throat size. However, the merging criterion of Delaunay tetrahedra at the 3D condition is rather subjective (Taylor et al. 2015), and is the main drawback of the DT method, as also noted in Table 1.

The MB method is often applied to extract the pore-throat network from the tomography images of rocks and sands (Silin et al. 2004; Al-Kharusi and Blunt 2007; Dong and Blunt 2009;

Arand and Hesser 2017). At each voxel coordinate of the image, an inscribed ball (i.e., the maximal ball) is constructed, and the radius of the maximal ball is the shortest distance to the solid phase. These balls are then merged into individual clusters, as schematically illustrated in Fig. 2b, using a 2D representation, where different colors are assigned to the clusters. The ball with a local minimum size in the cluster is denoted as a pore throat and the remaining ones are collectively considered as pores. Although the MB method is relatively objective in clustering (merging) the maximal balls, the associated voxelizations may lead to biases in characterizing the pore network, e.g., underestimating the throat size (Dong and Blunt 2009), producing tiny and incorrect throats ranging from 1~3 voxels (Shire et al. 2012) (see further discussion in Section 3), and producing throat surface by post-processing the maximal balls in the throat rather than the throat itself (e.g., Raeini et al. 2017). In addition to the DT and MB methods, different pore extraction methods, not limited to those for unconsolidated media, have also been proposed, such as the medial-axis-based method (Lindquist et al. 2000; Al-Raoush and Willson 2005), watershed method (Rabbani et al. 2014; Taylor et al 2015; Raeini et al. 2017), contact-based method (O'Sullivan et al. 2015) and others (Zhao et al. 1994; Øren and Bakke 2003; Okabe and Blunt 2004; Frenkel et al. 2009; Ngom et al. 2011; Yi et al. 2017). However, all of these methods still have their own pros and cons.

In light of above review, different proposed pore extraction methods might not render comparable and nonbiased results due to their own inherent limitations/disadvantages. This fact motivates us to explore a unified method, which, on the one hand, retains the advantages of these proposed methods, and on the other hand, minimizes (or even eliminates) the influence from the associated limitations/disadvantages, ultimately enabling the extraction of the pore-throat network in an objective and more accurate way. To achieve this goal, a novel method based on

unifying both the DT and MB methods is proposed herein. In Section 2, this proposed unified method is described in detail. In Section 3, the method is implemented on a sample (with a periodic boundary) subjected to triaxial shearing using DEM simulations. The associated evolution of pore network is then presented to demonstrate the merits of this unified method and for validation of its effectiveness. The key findings and future research directions are summarized in Section 4.

2. Methodology

The proposed method, as illustrated in Fig. 2, is based on unifying both the Delaunay tessellation (DT) and maximal ball (MB) methods. For ease of presentation, a 2D instead of 3D representation is used in Fig. 2, although the method is implemented in a 3D condition in this study. By combining these two methods, we can make the best use of the advantages of these two methods, as summarized in Table 1, and at the same time, minimize (or even eliminate) the influences from the associated disadvantages. Detailed description of this unified method is given below.

2.1. Step 1: construction of Delaunay tessellation

As shown in Fig. 2a, the whole space Ω, which can be classified into the solid phase Ω_s and pore phase Ω_v, is firstly partitioned into different Delaunay tetrahedra. Let $P=\{p_1, p_2 \ldots p_{n_p}\}$ be the set of solid particles in Ω. Here we target at the formulations for spherical particles. Let c_i and r_i be the centroid coordinate and radius of p_i, respectively. For a point $x \in \Omega$, the Laguerre distance to c_i is defined as

$$d_L(x,c_i)=d(x,c_i)^2-r_i^2 \tag{1}$$

where $d(x,c_i)=\|x-c_i\|_2$ is the Euclidean distance between x and c_i. Note that for the periodic boundary used in the case with DEM simulations used later on to evaluate this unified method, the modulo operation should be carried out, i.e., $(x-c_i)\equiv(x-c_i)\bmod L$, where L refers to the size of the periodic cell. Then, the radical Voronoi region for particle p_i can be constructed and defined as,

$$V(p_i)=\bigcap_{j}^{n_p}\{x\in\Omega|d_L(x,c_i)\le d_L(x,c_j),i\ne j\} \quad (2).$$

The Delaunay graph, as the dual of the radical Voronoi diagram, can be obtained by linking p_i and p_j, which have an adjacent Voronoi face. Essentially, tetrahedral meshes are generated on the particle centroids and each tetrahedron is associated with a Voronoi vertex. Then, let $Q=\{v_1,v_2\ldots v_{n_v}\}$ be the set of the Voronoi vertex; for v_i, the associated Delaunay region (tetrahedron) can be regarded as the set of particles whose Voronoi region shares this vertex, as

$$D(v_i)=\{p_j\in P|v_i\in V(p_j)\} \quad (3).$$

The Delaunay region can also be expressed as a continuum form. Let $D(v_i)=\{p_1,p_2\ldots p_{n_{v_i}}\}$ and the associated centroid coordinates be a set $\{c_1,c_2\ldots c_{n_{v_i}}\}$. The Delaunay region can then be written as

$$D'(v_i)=\left\{x\in\Omega|x=\sum_{j}^{n_{v_i}}\lambda_j c_j,\sum_{j}^{n_{v_i}}\lambda_j=1,0\le\lambda_j\le 1\right\} \quad (4).$$

Note that the Delaunay and Voronoi tessellation algorithms based on convex hull method are freely available in C++ (http://www.qhull.org) and have been widely implemented in most software (e.g., Matlab, Octave, R and Python).

2.2. Step 2: construction and clustering of maximal balls

As shown in Fig. 2b, construction and clustering of the maximal balls are then carried out. First, let $M = \{m_1, m_2 \ldots m_{n_m}\}$ be the set of maximal balls constructed in Ω. To achieve this goal, the whole space Ω is voxelized. Using the algorithm of Tompson et al. (2006), for each particle p_i, the associated boundary voxels can be identified as $x_{b,i}$. Then, at the voxel coordinate $x_k \in \Omega$, the maximal ball m_k and its radius r_k are given by

$$r_k(x_k) = \begin{cases} \min\limits_{b,i} \left\| x_k - x_{b,i} \right\|_2 & \text{if } x_k \in \Omega_{\mathrm{v}} \\ 0 & \text{if } x_k \in \Omega_{\mathrm{s}} \end{cases} \quad (5).$$

In addition to x_k and r_k, other attributes are also needed to describe the maximal ball m_k, and the associated data structure of m_k can be simply expressed as

$$m_k = \lfloor x_k \mid r_k \mid p_{k,i} \mid m_{k,\text{ancestor}} \mid m_{k,\text{parent}} \mid r_{k,\text{rank}} \mid l_{k,\text{throat}} \rfloor \quad (6)$$

where $p_{k,i}$ is the solid particle in contact with m_k, according to Eq. (5); $m_{k,\text{ancestor}}$ and $m_{k,\text{parent}}$ are the ancestor and parent maximal balls of m_k, respectively; and $r_{k,\text{rank}}$ is the ranking of m_k; $l_{k,\text{throat}}$ denotes m_k as a throat or not. Note that, initially, $m_{k,\text{ancestor}}$ and $m_{k,\text{parent}}$ are null, $r_{k,\text{rank}}$ is selected as a large integer to ease the raking of m_k, and $l_{k,\text{throat}}$ is set as false.

Then, the maximal balls are grouped into individual clusters, as illustrated in Fig. 2b with different colors, using the algorithm used in Dong and Blunt (2009). First, all the maximal balls are sorted in a descending order by r_k and stored in the list $L^{\downarrow r_k}$, where the downward arrow

denotes to order r_k in a descending way. $L^{\downarrow r_k}$ is traversed from the lowest ranking to the highest ranking. Using the following three rules, the attributes in m_k can be determined:

(i) m_k becomes the parent of its surrounding maximal ball m_l, when

$$\left\| x_k - x_j \right\|_2 \le r_k \text{ and } r_l \le r_k \tag{7}$$

and the attributes of m_l are updated by

$$\begin{cases} m_{l,\text{ancestor}} = m_{k,\text{ancestor}} \\ m_{l,\text{parent}} = m_k \\ r_{l,\text{rank}} = r_{k,\text{rank}} - 1 \end{cases} \tag{8}$$

(ii) If m_k has no parent, it becomes an ancestor (i.e., $m_{k,\text{ancestor}} = m_k$).

(iii) If the attribute $m_{k,\text{ancestor}}$ is accessed twice or more by a different cluster, m_k belongs to a throat (i.e., $l_{k,\text{throat}}$ = true).

After the traversal, all the maximal balls can find their own ancestors, parents and states of being a throat or not. The set of maximal balls that share the same ancestor (e.g., m_l) is then clustered together as,

$$S(M, m_l) = \{ m_k \in M \mid m_{k,\text{ancestor}} = m_l \} \tag{9}$$

2.3. Step 3: combination of DT and MB methods

For a specific cluster/set $S(M, m_l)$, the solid particles in contact with this cluster are first identified and denoted as

$$S(P, m_l) = \{ p_{k,i} \in P \mid m_k \in S(M, m_l) \} \tag{10}$$

As shown in Fig. 2c, the associated Delaunay tetrahedra, whose vertices are in the subset of those particles in contact with a particular cluster of maximal balls, are recognized and then merged together as a polyhedral void cell, i.e.,

$$R(m_l) = \{D'(v_i) | D(v_i) \subseteq S(P, m_l)\} \quad (11).$$

That is, merging Delaunay tetrahedra is no longer subjective and based on the areal porosity *n* of the common face, as often adopted. Instead, the clustering results of the MB method is leveraged to enable the associated merging process of Delaunay tetrahedra to become objective. It is worthwhile noting that the clustering process of the maximal balls is objective. In addition, as indicated in Fig. 2c (and Fig. 1d), these polyhedral void cells help precisely partition the pore space and define the throat size using the common faces between the polyhedral void cells.

In the next section, the procedures and merits of the unified method are further discussed through a numerical triaxial experiment. Also, the effectiveness of this method is evaluated, although the DT and MB methods have been individually validated, e.g., see Shire et al. (2012) and O'Sullivan et al. (2015).

3. Evaluation of the Unified Method

A granular sample subjected to triaxial shearing is first carried out using DEM simulation. Then, the process of pore network extraction using the unified method for this DEM sample is presented. Finally, comparisons are made between the pore-extraction results obtained from the unified method and those using the DT and MB methods in order to demonstrate the merit and effectiveness of the unified method.

3.1. Details of DEM simulation

The DEM software, PFC^{3D} 4.0 (Itasca Consulting Group, Inc., Minn.) was employed to generate the granular sample and model the process of triaxial shearing. We consider a monodisperse system using the periodic boundary here to exclude the additional influences from the particle-size distribution and boundary effect. The simulation process consists of the following three steps: (a) sample generation, (b) isotropic consolidation, and (c) triaxial shearing. To form the DEM sample, 680 spheres with radii of 0.005 m randomly were arranged into a periodic cell of a dimension $0.08 \times 0.08 \times 0.08$ m^3. According to Shire et al. (2012), this arrangement should be large enough to render stable statistical results of the pore structure. Subsequently, the sample was gradually compressed until an isotropic pressure of 100 kPa was reached. Fig. 3a shows the sample after consolidation, and the periodic boundary is set in three directions. The sample was finally subjected to triaxial shearing under constant confining stress. During shearing, the sample was continuously compressed in the z direction at a constant rate $\dot{\varepsilon}_z = 0.01\%/\sec$, which was sufficiently slow to maintain a quasi-static condition (Jop et al. 2006). In the x and y directions, the stress was kept constant at 100 kPa using the servo control algorithm given in Thorton (2000). The shearing process was completed when the shearing strain reached ε_z = 20%, and the sample after shearing is shown in Fig. 3b. Fig. 3c illustrates the stress-strain-volumetric response during the triaxial shearing, where shear-induced dilation can be observed. The packing solid fraction before shearing is 0.645, which is close to the value of a disordered close packing (Song et al. 2008). After shearing, the packing solid fraction drops to 0.570, with a coordination number of 4.68. This condition is near to a disordered loose packing (Song et al. 2008), in which, essentially, the sample has been sheared to unjamming. Note that some particles that have no contacts are generated by shearing, and they are excluded when calculating the packing fraction

and coordination number. However, they are still included in the analysis of pore-throat network, as they occupy the space and contribute to the permeability of the sample.

During the simulation process, a linear contact law, together with the Coulomb frictional criterion, was used to describe the contact behavior between particles. In this model, the parameters were chosen following the suggestions in Guo and Zhao (2014): the normal stiffness $k_n = 10^6$ N/m, the tangential stiffness $k_s = 0.75 \times 10^6$ N/m and the interparticle friction coefficient $\mu = 0.5$.

3.2. Pore network extraction using the unified method

As shown in Fig. 4a, the Voronoi diagram is constructed for the sample before shearing according to Eq. (2). Based on the Voronoi diagram (i.e., using Eq. (4)), the Delaunay tessellation is constructed on the particle centroids, as illustrated in Fig. 4b, and then, the maximal balls are constructed. First, as schematically illustrated in Fig. 5a, the sample is divided into 250^3 voxels. With such a resolution, each solid particle is represented by ~30^3 voxels, which is sufficient to produce reliable results when using the MB method, according to Shire (2012). For each voxel coordinate, if it is located at the pore space, the corresponding maximal ball is constructed using Eq. (5). Ultimately, the whole pore space is filled by the maximal balls, as shown in Fig. 5b. These balls are then grouped into clusters according to the method suggested in Dong and Blunt (2009) and each ball in the cluster shares the same ancestor (see Eq. (7)). To further elaborate this process, Fig. 6 presents three representative clustering cases. In each case, the clustering process starts with a ball having a relatively large radius as the ancestor of the cluster. The ancestor absorbs all the neighboring, overlapped smaller balls into cluster. The cluster grows by repeating this process on each newly absorbed ball, i.e., absorbing its neighboring, overlapped smaller balls into the cluster, until the ball has no smaller neighbor. Figs.

7a and 7b present the final clustering results of the maximal balls for the samples before and after shearing, respectively.

During the clustering process of the maximal balls, as the size of the cluster grows, it gradually touches more solid particles and penetrates into more Delaunay tetrahedra constructed in Fig. 4b. The tetrahedra penetrated by the same cluster are then identified and merged based on Eq. (9). Taking the cuiboid-like cluster (Fig. 6a) as an example, four Delaunay tetrahedra are merged to form an octahedral void cell to enclose the cluster (pores) as shown in Fig. 8a. For the tetrahedron-like clusters (Fig. 6b), one tetrahedron is sufficient to contain the cluster (Fig. 8b). For a complicated cluster (Fig. 6c), more Delaunay tetrahedra are required to merge to form a polyhedral void cell to surround the cluster (Fig. 8c). Eventually, the whole sample can be partitioned into different polyhedral cells, which enclose the pores (filled by the clusters) with pore throats passing through the common faces between the polyhedral cells.

3.3. Morphology of the pore space

As noted, the unified approach retains the advantages of both the DT and MB methods and minimizes the influence from the associated disadvantages, as summarized in Table 1; these particular merits are further revealed in the following discussion.

Since the Delaunay tessellation enables precise partitioning the pore space and clearly defining the throat size, the unified method offer a better descriptions of the pore-throat networks of the sample, as shown in Fig. 9, where the stick-ball model used in Al-Kharusi and Blunt (2007) and van der Linden et al. (2016) is adopted. The ball denotes the pore and the ball radius is proportional to the pore size. The stick denotes the connection between the pores and the stick radius is proportional to the throat size. The pore size can be defined as the radius of the

maximum inscribed ball in the pore (Øren and Bakke 2003; Al-Kharusi and Blunt 2007). Note that when using the DT method alone for the pore network extraction, further analyses are required; however, when using the unified method, the pore size is exactly the radius of the largest maximal ball (i.e., inscribed ball) in the associated cluster of maximal balls.

Figs. 10a and 10b show the probability density distributions of pore size before and after shearing, respectively, where the pore size R_{Pore} is normalized by the solid particle size R_{Part}. No pore has an observed size less than ~$0.2R_{\mathrm{Part}}$ because in the packing of mono-disperse, rigid spherical particles, the smallest pore size in theory is ~$0.22R_{\mathrm{Part}}$. It is also found that the number of small pores (i.e., those with $R_{\mathrm{Pore}} < 0.4R_{\mathrm{Part}}$) is significantly reduced by shearing. This is due to shear-induced dilation and the associated merging of pores as there are 1,288 pores before shearing and only 947 pores after shearing.

Fig. 11 shows the cumulative pre-shearing throat-size distribution of the sample before shearing obtained from the unified method, the DT method, and the MB method for comparison. For the unified method, as indicated in Fig. 1d, the throat size is defined as the radius of the inscribed circle on the face that the throat passes through. For the implementation of the DT method, the merging criterion for Delaunay tetrahedra proposed by van der Linden et al. (2016) is adopted, i.e., the adjacent Delaunay tetrahedra are merged when the common face has an areal porosity less than 0.4 (see Fig. 1c). The comparison shown in Fig. 11 reveals that the MB method underestimates the throat size, as also found in Dong and Blunt (2009). In addition, as also described in Shire et al. (2012), the MB method gives a tail of very tiny throats (around 1~3 voxels), which may bias the quantification of the throat size. As to the DT method, due to the selected merging criterion of the Delaunay tetrahedra, it generates a large number of throats, ~8,000, whereas the other two methods only produce ~5,000 throats. The unified method renders

the results between those obtained from the DT and MB methods. Most importantly, the effectiveness of the unified method is proven superior to the DT and MB methods since it avoids producing tiny and incorrect throats or too large throats.

Figs. 12a and 12b then present the probability density distributions of throat size before and after shearing, respectively, using the unified method, where the throat size R_{Throat} is also normalized by the particle size R_{Part}. Similar to the pore-size distribution, the throat size is also increased by shearing; however, the associated distribution pattern is different. The pore-size distribution before shearing is close to a gamma distribution, which is similar to the finding in Johnston (1998). However, the throat-size distribution before shearing follows an exponential-like distribution as also found in Sok et al. (2002). Once again, whether before or after shearing, very tiny throat ($R_{\mathrm{Throat}} < 0.15R_{\mathrm{Part}}$) and large throats ($R_{\mathrm{Throat}} > 0.6R_{\mathrm{Part}}$) are not observed, as theoretically predicted.

In addition to a better description of the pore space morphology, another advantage of using the unified method is the potential to explore a new dimension of fabric in granular systems, i.e., the fabric of the pore structure. This kind of fabric, e.g., in terms of the throat orientation, can affect the associated permeability (An et al. 2016) and therefore has been found to be important in the transport process during oil recovery (Behrouz et al. 2007; Rezaeipour et al. 2011). As the throat pass through the common face between the polyhedral void cells, its orientation can be well characterized using the outward normal of this face, as indicated in Fig. 1d. Therefore, the rose diagram can be applied to describe the probability density function $E(\theta,\phi)$ of the throat orientations (or the outward normals of the common face between the polyhedral void cells), with the constraint of

$$\int_0^{2\pi}\int_0^{\pi} E(\theta,\phi)\sin\theta \mathrm{d}\theta \mathrm{d}\phi = 1 \tag{12}$$

where θ and ϕ are the polar angle and azimuthal angle of the throat orientation, respectively. As shown in Fig. 13a, the throat normals do not have a preferred orientation before shearing since the sample is subjected to isotropic loading. However, after shearing due to increasing axial loading, the throat normals become more aligned in the horizontal direction (see Fig. 13b), implying that the pores shape is more elliptical like. This is similar to the findings from biaxial shearing in DEM simulation (Li and Li 2009; Kang et al. 2012; Fu and Dafalias 2015). Essentially, a shear-induced anisotropy is found on the throat-based fabric. Nevertheless, further examination on the use of the throat-based fabric is required.

4. Summary and Conclusion

In this study, a method to extract the pore network in granular or weakly consolidated media was developed, which unifies both the Delaunay tessellation (DT) and maximal balls (MB) methods in a complementary way. Hence, this unified method can retain the advantages of both methods, and, most importantly, can eliminate the disadvantages that occur when either the DT or MB method are used alone. That is, the clustering results of maximal balls is used to help improve the merging process of the Delaunay tetrahedra such that the whole pore space can be partitioned into many polyhedral void cells in an objective way, with the void cells containing the pores and the throat passing through the common faces between cells. In addition, the common problems involved in using the maximal balls method, i.e., underestimating the throat size and producing tiny and incorrect throats, can be eliminated by incorporating the Delaunay tessellation, which

enables precisely partitioning the pore space and clearly defining the throat size. In addition, the pore size can be directly obtained based on the radius of the maximum inscribed ball in the pore.

To further assess the merits and effectiveness of the proposed unified method, pore network extraction by this method was conducted on a sample (with periodic boundary) before and after triaxial shearing using DEM simulation. It was found that the unified method is objective and effective. The morphology of the pore space therefore can be accurately described in terms of the pore size, throat size and the associated distribution. Upon triaxial shearing, both the pore and throat sizes increase due to the dilation responses. The unified method can also help explore another dimension of fabric in granular media, i.e., the throat-based fabric, since the throat can be well identified. Before shearing, the throat normals do not exhibit a preferred orientation since the sample was subjected to isotropic loading; however, after shearing by increasing the axial loading, the throat normals align more in the horizontal direction. Still, it has to be noted that there is a trade-off between the effectiveness and the time cost; in this case, the computational time is ~25 min using Intel® Core™ i5 CPU, which is 15% more than that by the MB method.

However, real sample is usually composed of poly-disperse, no-spherical particles, and difficulties must occur when applying this unified method to the general case. For instance, as reported by Medvedev et al. (2008) in the assembly of poly-disperse spheres, when the particle size is widely distributed, the construction of Delaunay graph may be problematic. Specifically, some Delaunay cells may superimpose, and adjustments have to be made on these cells. Distorted cells are also reported by Shi et al. (2013); these cells connecting between tiny and large particles may be wrongly identified as pore openings. However, with the help of MB method, such kind of mistakes may be eliminated. Still, more discussions are needed on how to

handle with the tiny particles, when applying the unified method to the case of poly-disperse particles. Then, to extend the application to non-spherical particles, difficulties are again on constructing the Delaunay graph. The burn algorithm in Tompson et al. (2006) can be first applied, as it helps to identify the particle position and boundary in the tomography image. Next, for each identified particle, the Voronoi region can be established using the Set Voronoi algorithm (Schaller et al. 2013; Dong et al. 2016); its dual, the Delaunay graph, can be constructed thereafter. It is expected that under these preparations, the DT and MB methods can be unified for pore network extraction. In all these regards, future study therefore would focus on tackling these problems and generalizing the unified method to the network extraction for real granular media.

Acknowledgments

This research was supported by the Hong Kong Research Grants Council (project no. T22-603/15-N) and Hong Kong PhD Fellowship Scheme (HKPFS). The authors are also grateful to the reviewers for their valuable comments.

ACCEPTED MANUSCRIPT

References

Al-Kharusi, A.S., Blunt, M.J., 2007. Network extraction from sandstone and carbonate pore space images. J. Pet. Sci. Eng. 56(4), 219-231.

Al-Raoush, R.I., Thompson, K., Willson, C.S., 2003. Comparison of network generation techniques for unconsolidated porous media. Soil Sci. Soc. Am. J. 67(6), 1687-1700.

Al-Raoush, R.I., Willson, C.S., 2005. Extraction of physically realistic pore network properties from three-dimensional synchrotron X-ray microtomography images of unconsolidated porous media systems. J. Hydrol. 300(1), 44-64.

An, S., Yao, J., Yang, Y., Zhang, L., Zhao, J., Gao, Y., 2016. Influence of pore structure parameters on flow characteristics based on a digital rock and the pore network model. J. Nat. Gas. Sci. Eng. 31, 156-163.

Arand, F., Hesser, J., 2017. Accurate and efficient maximal ball algorithm for pore network extraction. Comput. Geosci. 101, 28-37

Behrouz, R., Kharrat, R., Ghazanfari, M.H., 2007. Experimental study of factors affecting heavy oil recovery in solvent floods. In: Canadian International Petroleum Conference, Canada.

Bourg, I.C., Bourg, A.C.M., Sposito, G., 2003. Modeling diffusion and adsorption in compacted bentonite: a critical review. J. Contam. Hydrol. 61(1), 293-302.

Bryant, S., Blunt, M.J., 1992. Prediction of relative permeability in simple porous media. Phys. Rev. A 46(4), 2004-2011.

Coop, M.R., Willson, S.M., 2003. Behavior of hydrocarbon reservoir sands and sandstones. J. Geotech. Geoenviron. Eng. 129(11), 1010-1019.

Cui, Y., Nouri, A., Chan, D., Rahmati, E., 2016. A new approach to DEM simulation of sand production. J. Pet. Sci. Eng. 147, 56-67.

Burdine, N., 1993. Relative permeability calculations from pore size distribution data. J. Pet. Technol. 5(3), 71-78.

David, C., Wong, T.F., Zhang, J., 1994. Laboratory measurement of compaction-induced permeability change in porous rocks: Implications for the generation and maintenance of pore pressure excess in the crust. Pure Appl. Geophys. 143(1), 425-456.

Das, A., Kumar, A., 2017. Evolution of pore size distribution in deforming granular materials. Géotechnique Lett. 7(1), 24-29.

Dong, H., Blunt, M.J., 2009. Pore-network extraction from micro-computerized-tomography images. Phys. Rev. E 80, 036307.

Dong, K., Wang, C., Yu, A., 2016. Voronoi analysis of the packings of non-spherical particles. Chem. Eng. Sci. 153, 330-343.

Dullien, F.A.L., 1992. Porous Media-Fluid transport and Porous Structure. Academic Press, Inc, San Diego.

Fishman, Z., Bazylak, A., 2011. Heterogeneous through-plane porosity distributions for treated PEMFC GDLs I. PTFE effect. J. Electrochem. Soc. 158(2), B841-B845.

Frenkel, G., Blumenfeld, R., King, P.R., Blunt, M.J., 2009. Topological analysis of foams and tetrahedral structures. Adv. Eng. Mater. 11(3), 169-176.

Fu. P., Dafalias, Y.F., 2015. Fabric evolution within shear bands of granular materials and its relation to critical state theory. Int. J. Solid Struct. 63, 1918-1948.

Gao, Z., Hu, Q., 2013. Estimating permeability using median pore-throat radius obtained from mercury intrusion porosimetry. J. Geophys. Eng. 10(2), 025014.

Garboczi, E.J., 2002. Three-dimensional mathematical analysis of particle shape using X-ray tomography and spherical harmonics: Application to aggregates used in concrete. Cem. Concr. Res. 32(10), 1621-1638.

Ghanizadeh, A., Clarkson, C.R., Aquino, S., Ardakani, O.H., Sanei, H., 2015. Petrophysical and geomechanical characteristics of Canadian tight oil and liquid-rich gas reservoirs: I. Pore network and permeability characterization. Fuel 153, 664-681.

Ghassemi, A., Pak, A., 2011. Pore scale study of permeability and tortuosity for flow through particulate media using lattice Boltzmann method. Int. J. Numer. Anal. Met. 35(8), 886-901.

Gladkikh, M., Bryant, S.L., 2006. Influence of wettability on petrophysical properties during imbibition in a random dense packing of equal spheres. J. Pet. Sci. Eng. 52(1), 19-34.

Guo, N., Zhao, J., 2014. Local fluctuations and spatial correlations in granular flows under constant-volume quasistatic shear. Phys. Rev. E 89, 042208.

Johnston, P.R., 1998. Revisiting the most probable pore-size distribution in filter media: the gamma distribution Filtr. Sep. 35(3), 287-292.

Jop, P., Forterre, Y., Pouliquen, O., 2006. A constitutive law for dense granular flows. Nature 441(7094), 727-730.

Juang, C.H., Holtz, R.D., 1986. Fabric, pore size distribution, and permeability of sandy soils. J. Geotech. Eng. 112(9), 855-868.

Kang, D.H., Lee, J.H., Choo, J., Yun, T.S., 2012. DEM simulation on soil creep and associated evolution of pore characteristics. Comput. Geotech. 39, 98-106.

Kang, D.H., Yun, T.S., Kim, K.Y., Jang, J., 2016. Effect of hydrate nucleation mechanisms and capillarity on permeability reduction in granular media. Geophys. Res. Lett. 43(17), 9018-9025.

Lala, A.M.S., & El-Sayed, N.A., 2017. Controls of pore throat radius distribution on permeability. J. Pet. Sci. Eng. 157, 941-950.

Li, X., Li, X.S., 2009. Micro-macro quantification of the internal structure of granular materials. J. Eng. Mech. 135(7), 641-656.

Lindquist, W.B., Venkatarangan, A., Dunsmuir, J., Wong, T.F., 2000. Pore and throat size distributions measured from synchrotron X-ray tomographic images of Fontainebleau sandstones. J. Geophys. Res. Solid Earth 105(B9), 21509-21527.

Medvedev, N.N., Voloshin, V.P., Luchnikov, V.A., Gavrilova, M.L., 2006. An algorithm for three-dimensional Voronoi S-network. J. Comput. Chem. 27(14), 1676-1692.

Meng, Y., Li, Z., Lai, F., 2015. Experimental study on porosity and permeability of anthracite coal under different stresses. J. Pet. Sci. Eng. 133, 810-817.

Niu, Q., Revil, Z., Li, Z., Wang, Y.H., 2017. Relationship between electrical conductivity anisotropy and fabric anisotropy in granular materials during drained triaxial compressive tests: a numerical approach. Geophys. J. Int. 210(1), 1-17.

Ngom, N.F., Garnier, P., Monga, O., Peth, S., 2011. Extraction of three-dimensional soil pore space from microtomography images using a geometrical approach. Geoderma 163(1), 127-134.

Okabe, H., Blunt, M.J., 2004. Prediction of permeability for porous media reconstructed using multiple-point statistics. Phys. Rev. E 70, 066135.

Øren, P.E., Bakke, S., 2003. Reconstruction of Berea sandstone and pore-scale modelling of wettability effects. J. Pet. Sci. Eng. 39(3), 177-199.

O'Sullivan, C., Bluthé, C.J., Sejpar, K., Shire, T., Cheung, L.Y.G., 2015. Contact based void partitioning to assess filtration properties in DEM simulations. Comput. Geotech. 64, 120-131.

Rabbani, A., Jamshidi, S., Salehi, S., 2014. Dynamic modeling of the formation damage and mud cake deposition using filtration theories coupled with SEM image processing. J. Pet. Sci. Eng. 123, 157-168.

Raeini, A.Q., Bijelic, B., Blunt, M.J., 2017. Generalized network modeling: Network extraction as a coarse-scale discretization of the void space of porous media. Phys. Rev. E 96, 013312.

Rashid, F., Glover, P., Lorinczi, W.J.P., Hussein, D., Lawrence, J.A., 2017. Microstructural controls on reservoir quality in tight oil carbonate reservoir rocks. J. Pet. Sci. Eng. 156 (2017), 814-826.

Reboul, N., Vincens, E., Cambou, B., 2008. A statistical analysis of void size distribution in a simulated narrowly graded packing of spheres. Granul. Matt. 10(6), 457-468.

Reboul, N., Vincens, E., Cambou, B., 2010. A computational procedure to assess the distribution of constriction sizes for an assembly of spheres. Comput. Geotech. 37(1), 195-206.

Rezaee, M.R., Jafari, A., Kazemzadeh, E., 2006. Relationships between permeability, porosity and pore throat size in carbonate rocks using regression analysis and neural networks. J. Geophys. Eng. 3(4), 370-376.

Rezaeipour, A.R., Kharrat, R., Ghazanfari, M.H., Yasari, E., 2011. The Role of Throat Orientation on Dispersion of Solvent in Crude Oil-Saturated Porous Media. Pet. Sci. Technol. 29(6), 649-663.

Rong, L.W., Dong, K.J., Yu, A.B., 2013. Lattice-Boltzmann simulation of fluid flow through packed beds of uniform spheres: Effect of porosity. Chem. Eng. Sci. 99, 44-58.

Schaller, F.M., Kapfer, S.C., Evans, M.E., Hoffmann, M.J., Aste, T., Saadatfar, M., Mecke, K., Delaney, G.W., Schröder-Turk, G.E., 2013. Set Voronoi diagrams of 3D assemblies of aspherical particles. Philos. Mag. 93(31), 3993-4017.

Shi, X., Prodanović, M., Holder, J., Gray, K.E., DiCarlo, D., 2013. Coupled solid and fluid mechanics modeling of formation damage near wellbore. *J. Petrol. Sci. Eng.* 112, 88-96.

Shire, T., O'Sullivan, C., Gaudray, G., 2012. Comparison of two methods for measurement of soil constriction size distribution. In: Proceeding of the Sixth International Conference on Scour and Erosion, Paris.

Silin, D.B., Jin, G., Patzek, T.W., 2004. Robust determination of the pore space morphology in sedimentary rocks. J. Pet. Technol. 56(5), 69-70.

Song, C., Wang, P., Makse, H.A., 2008. A phase diagram for jammed matter. Nature 453(7195), 629-632.

Sok, R.M., Knackstedt, M.A., Sheppard, A.P., Pinczewski, W.V., Lindquist, W.B., Venkatarangan. A., Paterson, L., 2002. Direct and stochastic generation of network models from tomographic images; effect of topology on residual saturations. Transport Porous Med. 46(2), 345-371.

Sun, W.C., Kuhn, M.R., Rudnicki, J.W., 2013. A multiscale DEM-LBM analysis on permeability evolutions inside a dilatant shear band. Acta Geotech. 8(5), 465-480.

Taylor, H.F., O'Sullivan, C., Sim, W.W., 2015. A new method to identify void constrictions in micro-CT images of sand. Comput. Geotech. 69, 279-290.

Thompson, K.E., Willson, C.S., Zhang, W., 2006. Quantitative computer reconstruction of particulate materials from microtomography images. Powder Technol. 163(3), 169-182.

Thorton, C., 2000. Numerical simulations of deviatoric shear deformation of granular media Géotechnique 50(1), 43-53.

van der Linden, J.H., Narsilio, G.A., Tordesillas, A., 2016. Machine learning framework for analysis of transport through complex networks in porous, granular media: A focus on permeability. Phys. Rev. E 94, 022904.

Wang, X., Zhang, M., Jivkov, A.P., 2016. Computational technology for analysis of 3D meso-structure effects on damage and failure of concrete. Int. J. Solid Struct. 80, 310-333.

Xiong, Q., Baychev, T.G., Jivkov, A.P., Review of pore network modelling of porous media: experimental characterisations, network constructions and applications to reactive transport. J. Contam. Hydrol. 192, 101-117.

Yi. Z., Lin, M., Jiang, W., Zhang, Z., Li, H., 2017. Pore network extraction from pore space images of various porous media systems. Water Resour. Res. 53(4), 3424-3445.

Zhao, H.Q., Macdonald, I.F., Kwiecien, M.J., 1994. Multi-orientation scanning: a necessity in the identification of pore necks in porous media by 3-D computer reconstruction from serial section data. J. Colloid Interf. Sci. 162, 390-401.

Zhu, W., Wong, T., 1997. The transition from brittle faulting to cataclastic flow: Permeability evolution. J. Geophys. Res. Solid Earth 102(B2), 3027-3041.

ACCEPTED MANUSCRIPT

ACCEPTED MANUSCRIPT

List of Tables

Table 1 Brief descriptions of the Delaunay tessellation method and maximal ball method and a summary of the associated advantages and disadvantages.

ACCEPTED MANUSCRIPT

ACCEPTED MANUSCRIPT

Table 1 Brief descriptions of the Delaunay tessellation method and maximal ball method and a summary of the associated advantages and disadvantages.

Method	Description	Advantages	Disadvantage
Delaunay tessellation method (DT)	• Construct Delaunay tessellation on particle centroids • Merge adjacent tetrahedra when their common face does not represent a void boundary	• Precisely partition the pore space to set the boundary between pores and clearly define the throat size	• Have a subjective criterion for merging the Delaunay tetrahedra
Maximal ball method (MB)	• Construct a maximal ball on each voxel in the pore space • Group the maximal balls into individual clusters	• Have an objective clustering (merging) criterion for maximal balls • Directly provide the pore size (radius)	• Underestimate the throat size • Produce tiny and incorrect throats

ACCEPTED MANUSCRIPT

List of Figures

Fig. 1 Merging criterion of Delaunay tetrahedra used in van der Linden et al. (2016): (a) four spherical particles; (b) two associated Delaunay tetrahedra; (c) the areal porosity *n* of the common face indicated in (b) (when *n* exceeds 0.4, the two tetrahedra will be merged); and (d) the corresponding pore and throat given by the Delaunay tessellation method.

Fig. 2 Schematic illustration of the unified method: (a) step 1: construction of the Delaunay tessellation on the particle centroids; (b) step 2: construction and clustering of the maximal balls (the balls in blue); (c) step 3: combining the DT and MB methods, i.e., merging of Delaunay cells prompted by clustering result of maximal balls. For instance, the two left Delaunay cells are merged as they are penetrated by the same dark blue cluster.

Fig. 3 DEM simulation: (a) the sample before shearing (with periodic boundary); (b) the sample after shearing; and (c) the stress-strain-volumetric responses.

Fig. 4 Construction of Delaunay tessellation on the sample before shearing: (a) the Voronoi diagram and (b) Delaunay tessellation on the particle controids.

Fig. 5 Construction of maximal balls on the sample before shearing: (a) the schematic voxelization and (b) the maximal balls at all the voxel coordinates. Note that the sample is actually divided into 250^3 voxels

Fig. 6 Clustering of maximal balls in three representative cases: (a) a cuboid-like cluster; (b) a tetrahedron-like cluster; and (c) a more complicated cluster. The clustering process starts with the maximal balls with a relative large radius (the second column). Their neighboring, overlapped smaller balls are absorbed into cluster. The same absorbing process is repeated on every newly absorbed ball until the ball has no smaller neighbor (the last column).

Fig. 7 Clustering results of the maximal balls for the sample: (a) before shearing and (b) after shearing.

Fig. 8 Merging of Delaunay tetrahedra in three representative cases: (a) a cuboid-like cluster; (b) a tetrahedron-like cluster; and (c) a more complicated cluster.

Fig. 9 Pore-throat network: (a) before shearing and (b) after shearing.

Fig. 10 Probability density distribution of pore size: (a) before shearing and (b) after shearing.

Fig. 11 Cumulative throat-size distributions of the sample before shearing, obtained from the DT method, the MB method and the unified method.

Fig. 12 Probability density distribution of throat size: (a) before shearing and (b) after shearing.

Fig. 13 Orientational distribution of the throat normals: (a) before shearing and (b) after shearing.

ACCEPTED MANUSCRIPT

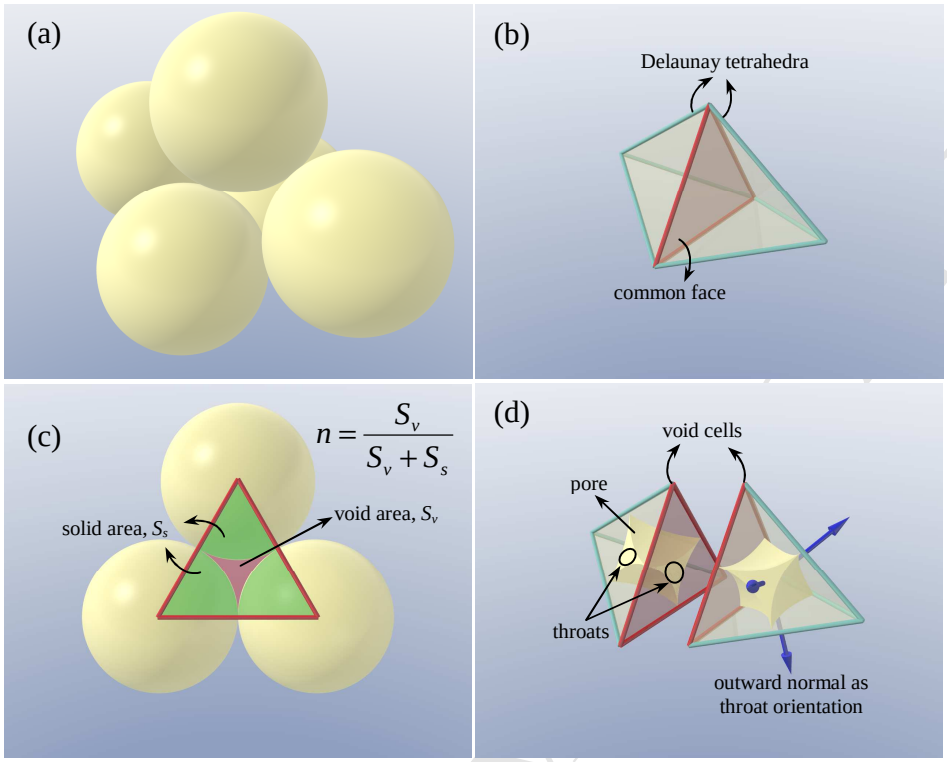

Fig. 1 Merging criterion of Delaunay tetrahedra used in van der Linden et al. (2016): (a) four spherical particles; (b) two associated Delaunay tetrahedra; (c) the areal porosity n of the common face indicated in (b) (when n exceeds 0.4, the two tetrahedra will be merged); and (d) the corresponding pore and throat given by the Delaunay tessellation method.

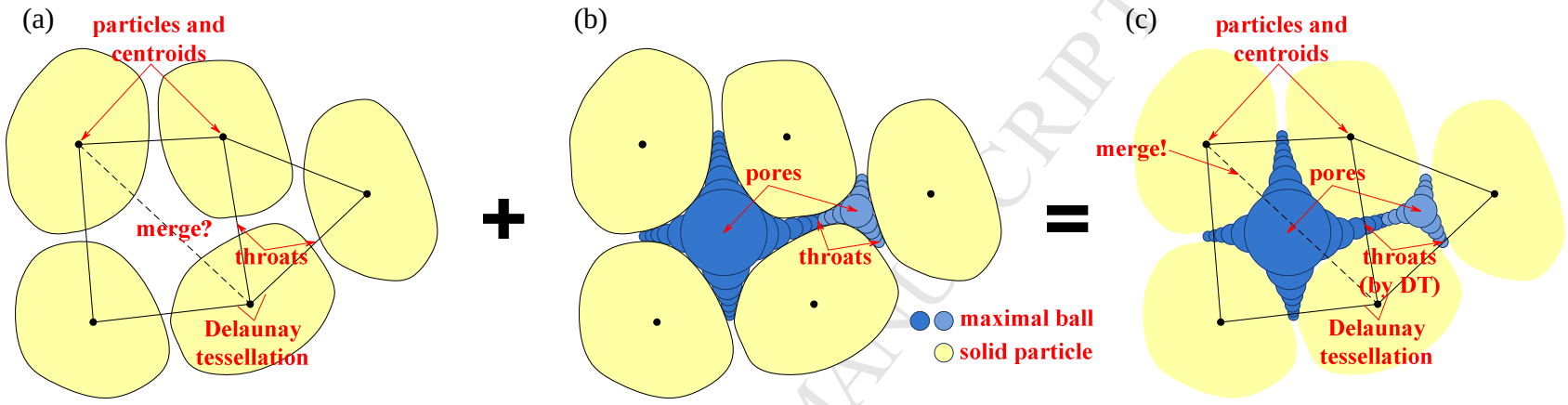

Fig. 2 Schematic illustration of the unified method: (a) step 1: construction of the Delaunay tessellation on the particle centroids; (b) step 2: construction and clustering of the maximal balls (the balls in blue); (c) step 3: combining the DT and MB methods, i.e., merging of Delaunay cells prompted by clustering result of maximal balls. For instance, the two left Delaunay cells are merged as they are penetrated by the same dark blue cluster.

ACCEPTED MANUSCRIPT

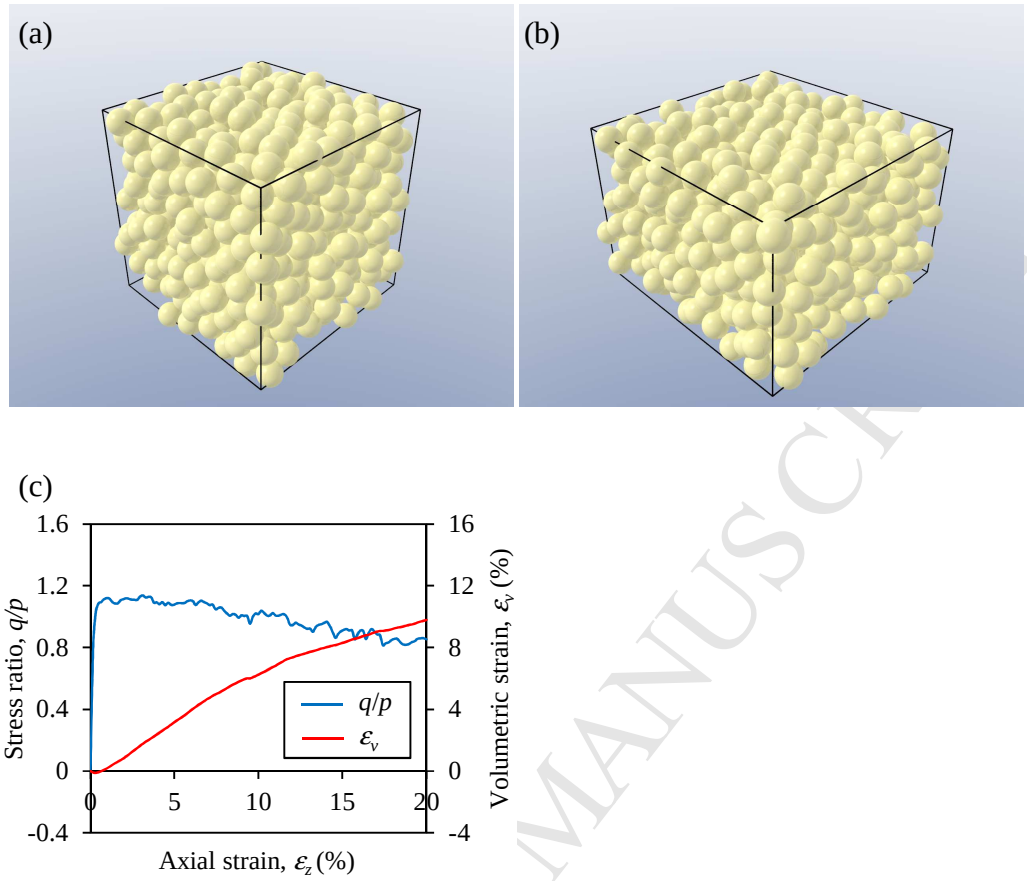

Fig. 3 DEM simulation: (a) the sample before shearing (with periodic boundary); (b) the sample after shearing; and (c) the stress-strain-volumetric responses.

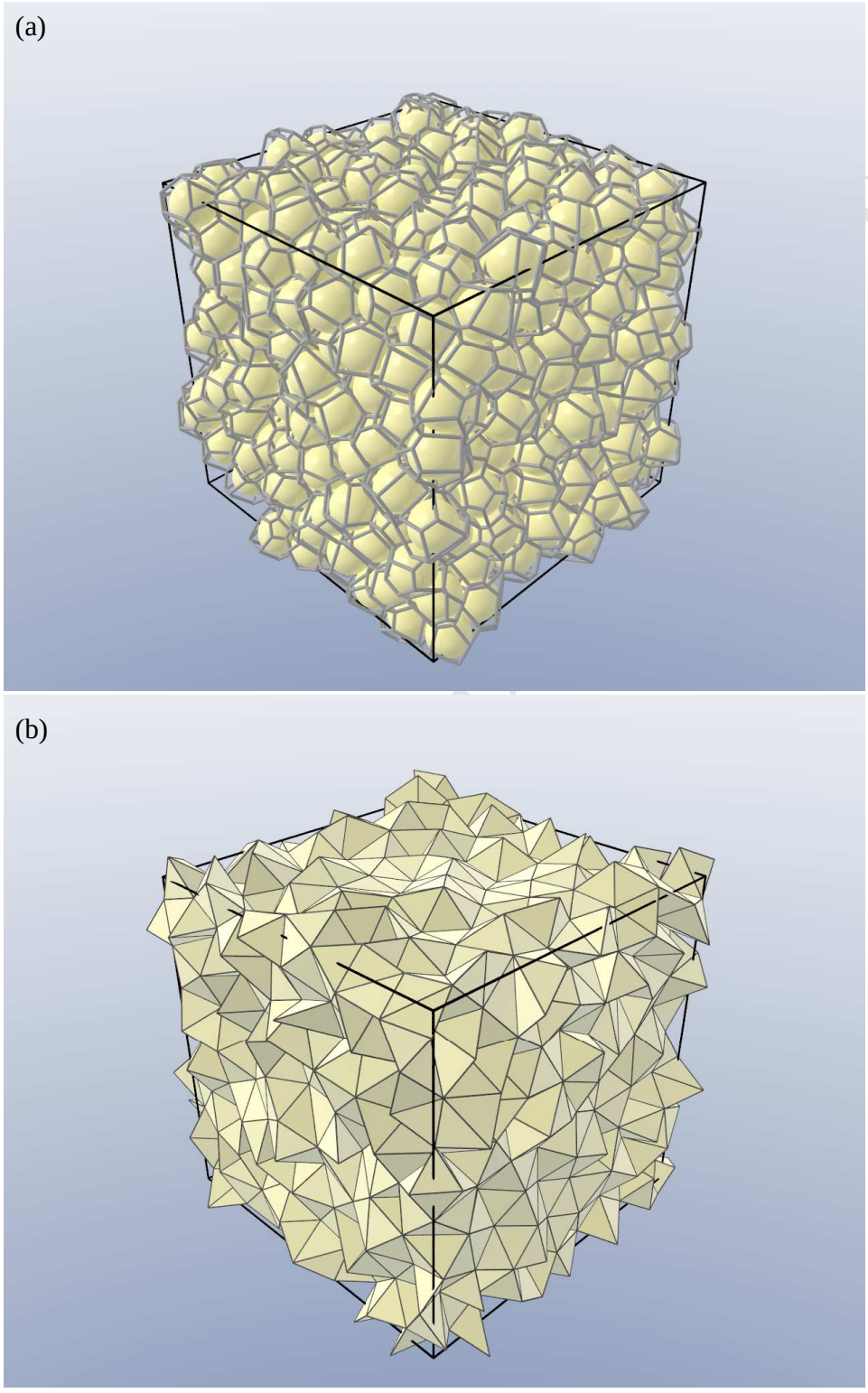

Fig. 4 Construction of Delaunay tessellation on the sample before shearing: (a) the Voronoi diagram and (b) Delaunay tessellation on the particle controids.

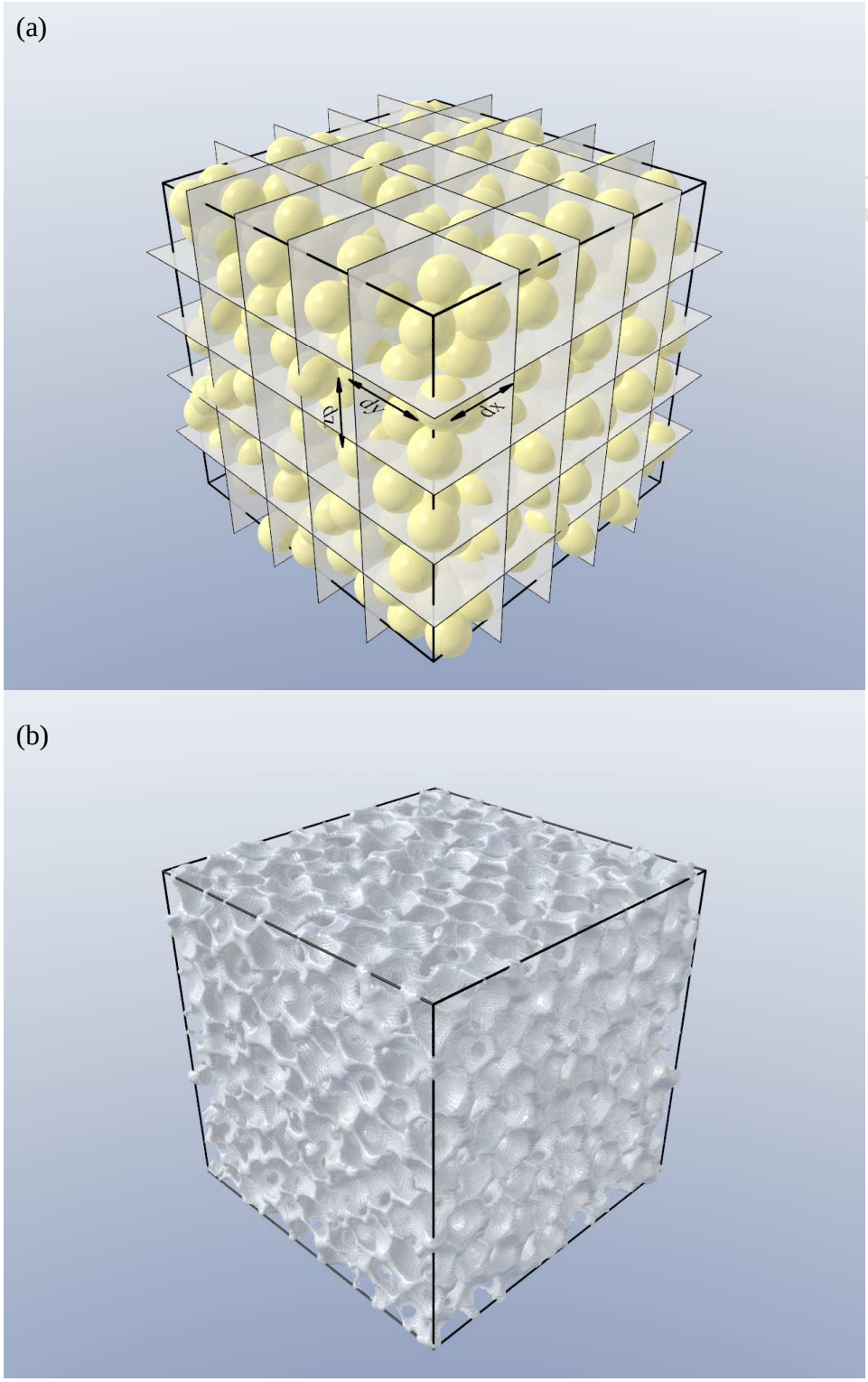

Fig. 5 Construction of maximal balls on the sample before shearing: (a) the schematic voxelization and (b) the maximal balls at all the voxel coordinates. Note that the sample is actually divided into 250^3 voxels

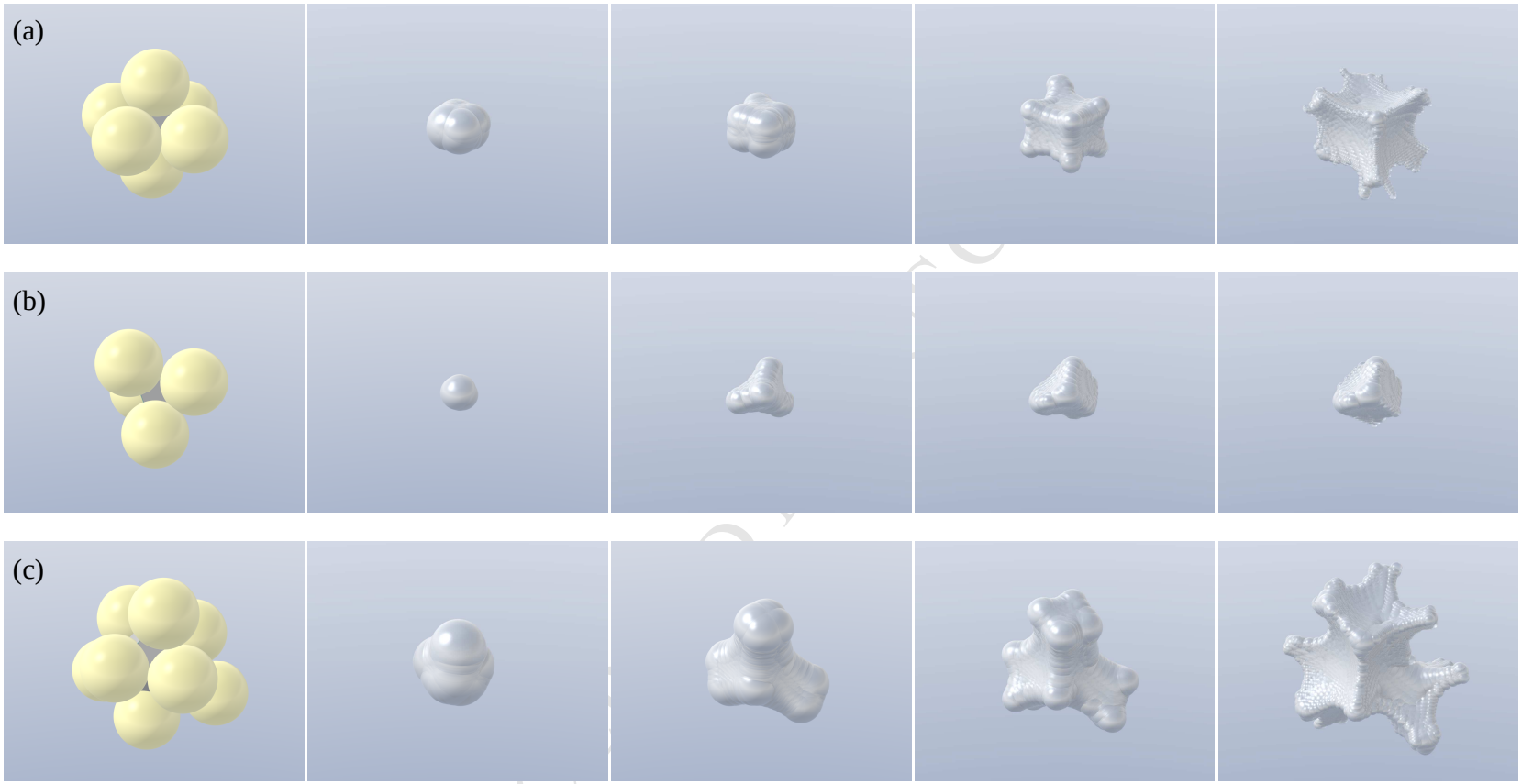

Fig. 6 Clustering of maximal balls in three representative cases: (a) a cuboid-like cluster; (b) a tetrahedron-like cluster; and (c) a more complicated cluster. The clustering process starts with the maximal balls with a relative large radius (the second column). Their neighboring, overlapped smaller balls are absorbed into cluster. The same absorbing process is repeated on every newly absorbed ball until the ball has no smaller neighbor (the last column).

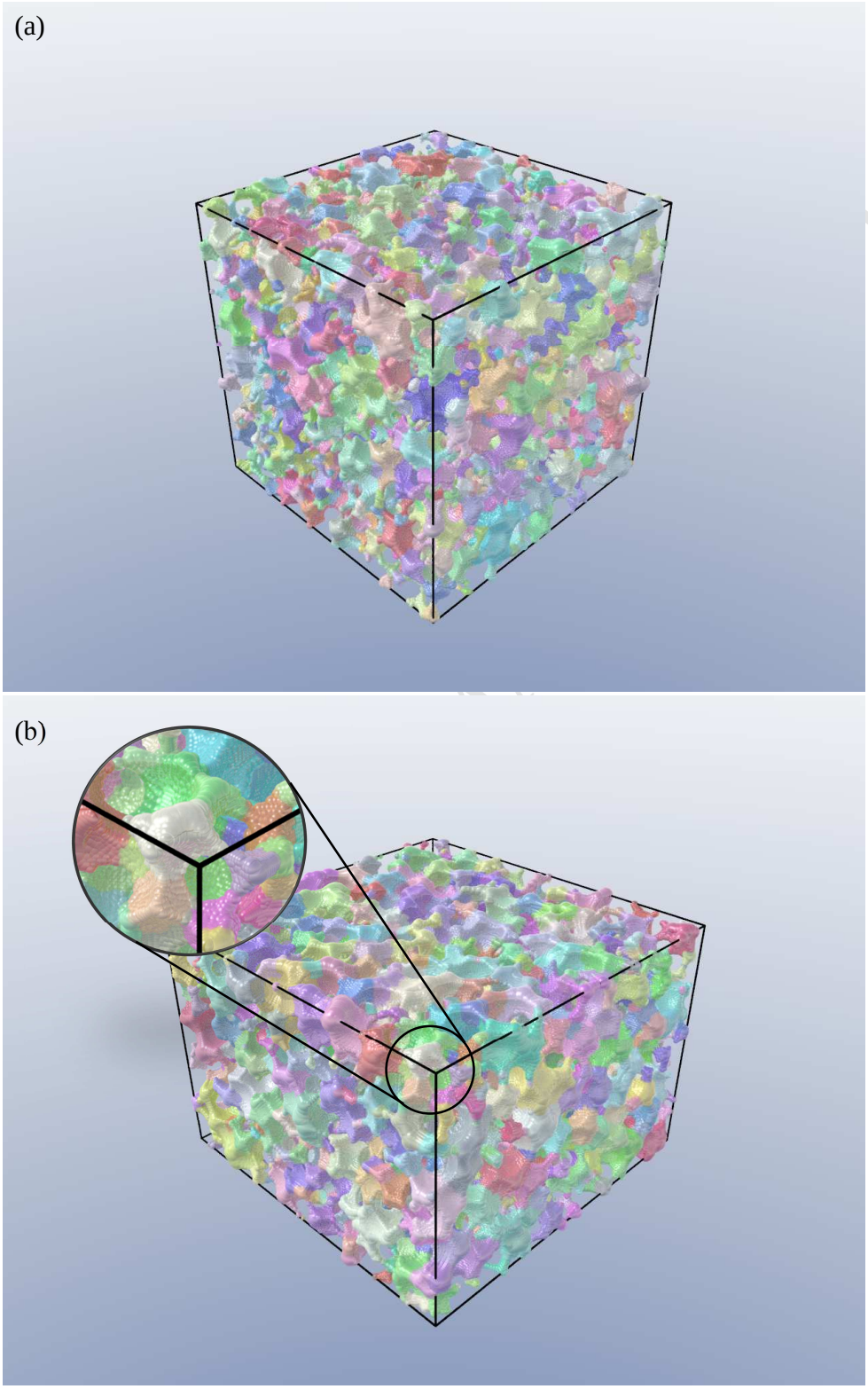

Fig. 7 Clustering results of the maximal balls for the sample: (a) before shearing and (b) after shearing.

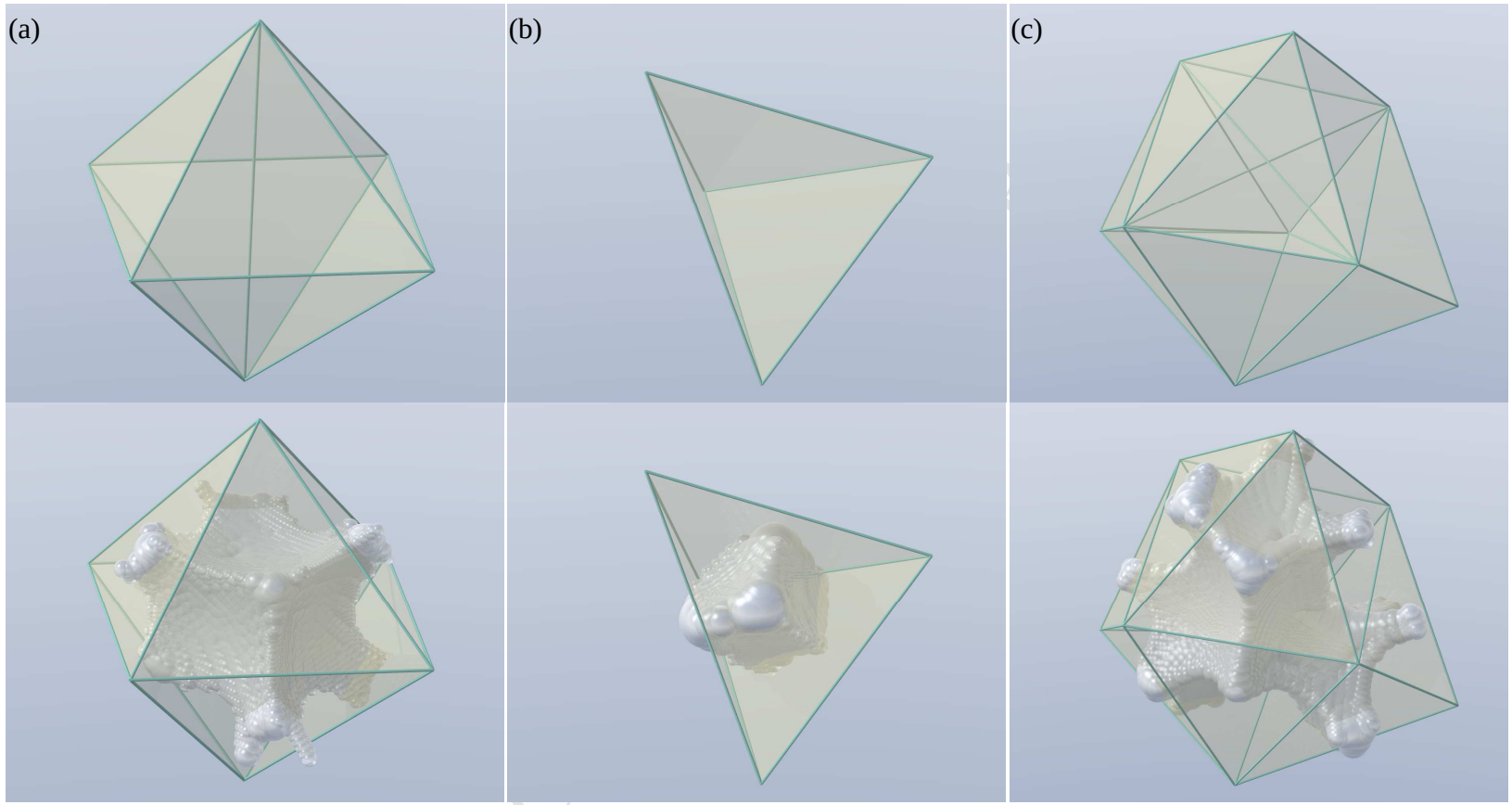

Fig. 8 Merging of Delaunay tetrahedra in three representative cases: (a) a cuboid-like cluster; (b) a tetrahedron-like cluster; and (c) a more complicated cluster.

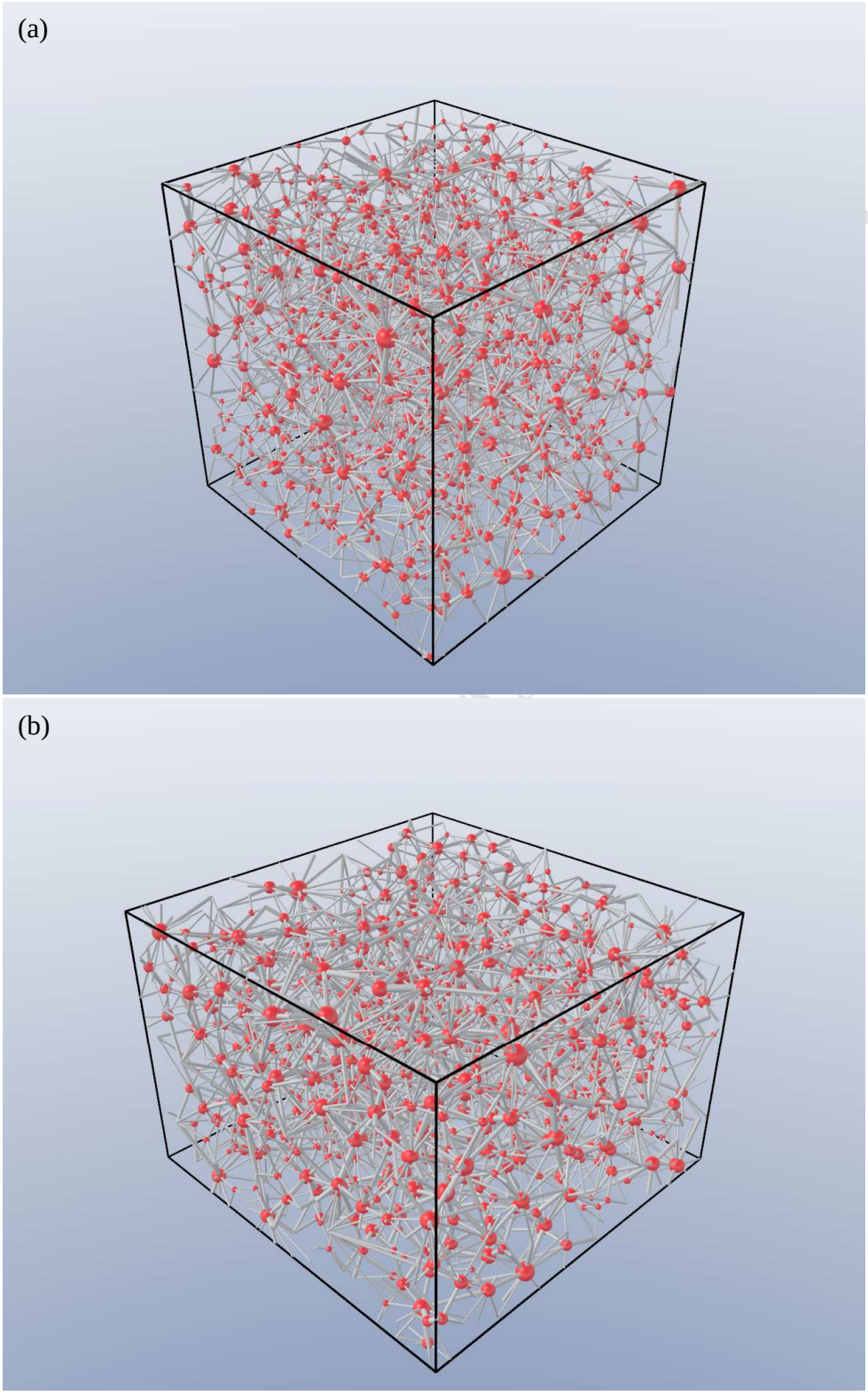

Fig. 9 Pore-throat network: (a) before shearing and (b) after shearing.

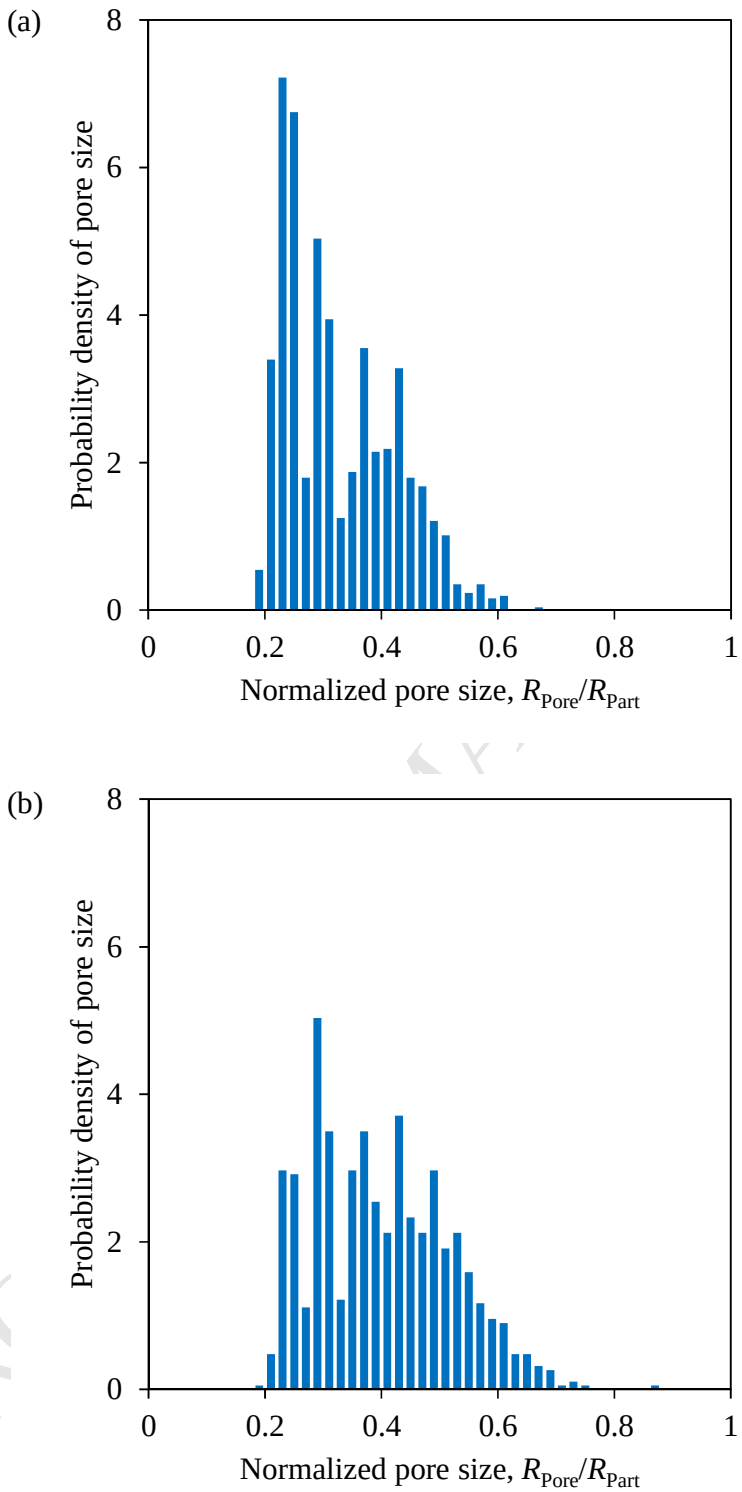

Fig. 10 Probability density distribution of pore size: (a) before shearing and (b) after shearing.

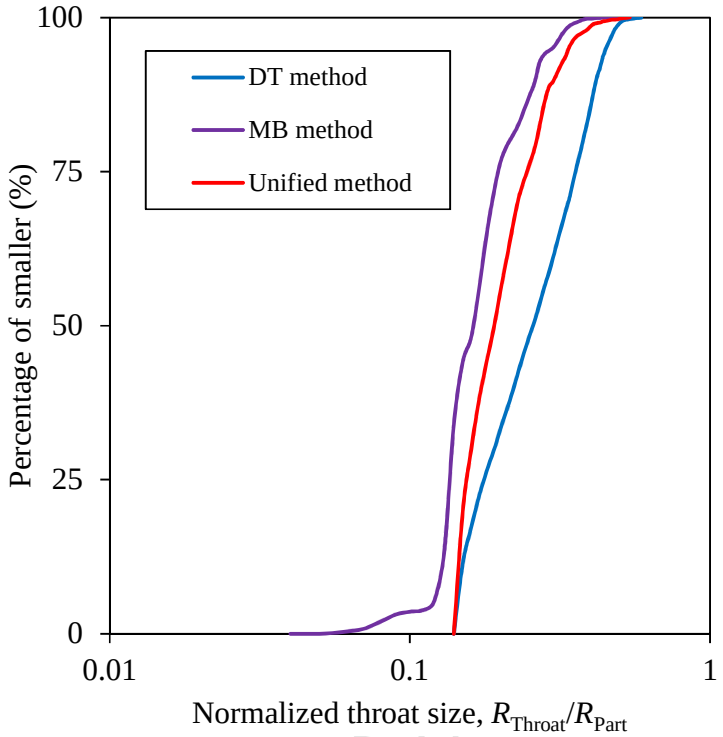

Fig. 11 Cumulative throat-size distributions of the sample before shearing, obtained from the DT method, the MB method and the unified method.

ACCEPTED MANUSCRIPT

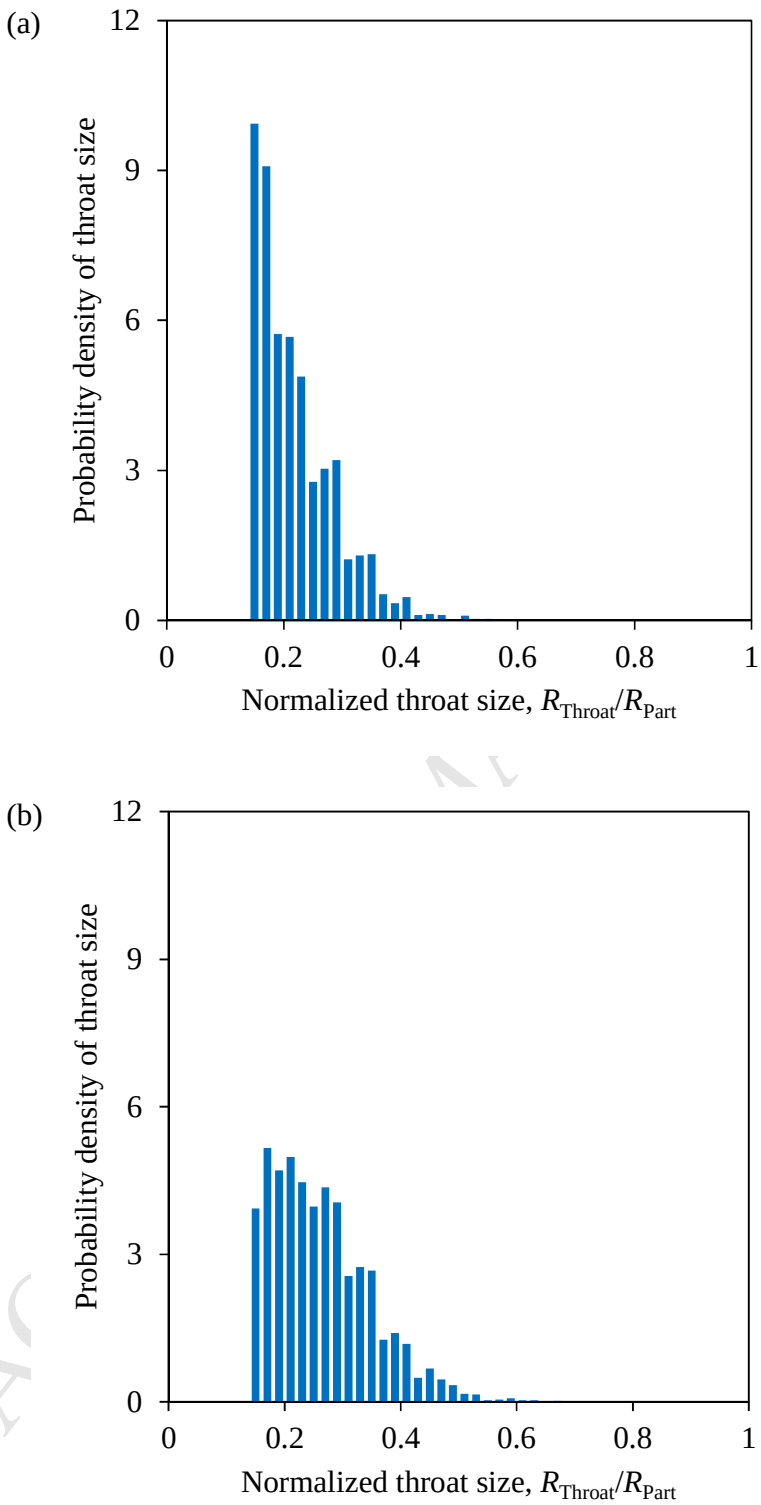

Fig. 12 Probability density distribution of throat size: (a) before shearing and (b) after shearing.

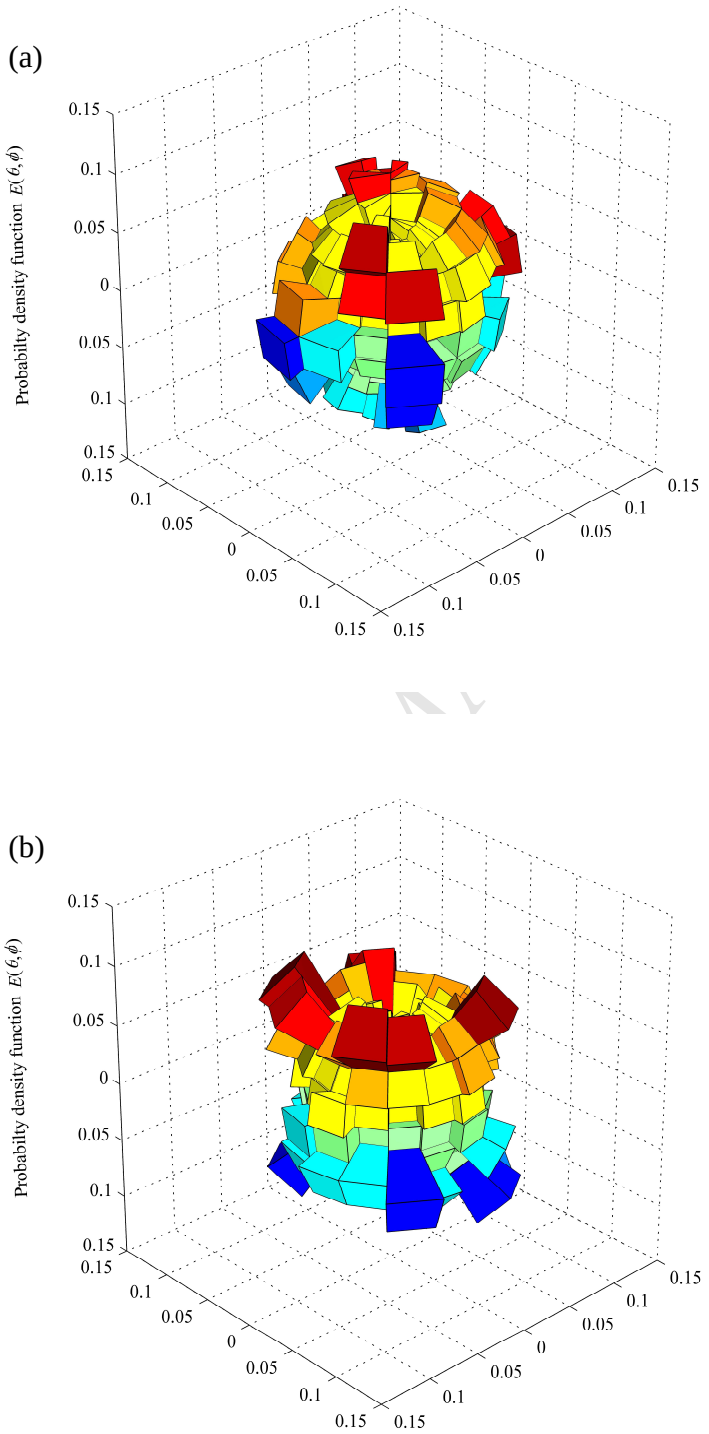

Fig. 13 Orientational distribution of the throat normals: (a) before shearing and (b) after shearing.

ACCEPTED MANUSCRIPT

Highlights

- Pore network is extracted by unifying Delaunay tessellation and maximal ball methods.
- Pore space is partitioned into individual polyhedral void cells objectively.
- Pores are contained in void cells and throats pass through common faces between cells.
- Both pore and throat sizes are increased by shearing due to the dilation response.
- After triaxial shearing, throat normals align more in the horizontal direction.

ACCEPTED MANUSCRIPT